NANO LETTERS
Letter
pubs.acs.org/NanoLett

Interface Magnetism in Epitaxial $BiFeO_3$-$La_{0.7}Sr_{0.3}MnO_3$ Heterostructures Integrated on Si(100)

S. S. Rao,[†,‡,*] J. T. Prater,[†,‡] Fan Wu,[‡] C. T. Shelton,[‡] J.-P. Maria,[‡] and J. Narayan[‡]

[†]Materials Science Division, Army Research Office, Research Triangle Park, North Carolina 27709, United States
[‡]Department of Materials Science and Engineering, North Carolina State University, Raleigh, North Carolina 27695, United States

S Supporting Information

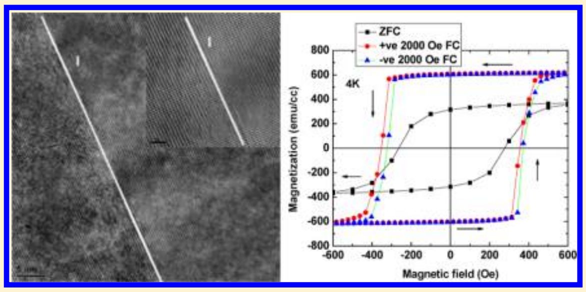

ABSTRACT: We report on the heteroepitaxial growth of ferroelectric (FE)-antiferromagnetic (AFM) $BiFeO_3$ (BFO) on ferromagnetic $La_{0.7}Sr_{0.3}MnO_3$ (LSMO), integrated on Si(100) using pulsed laser deposition via the domain matching epitaxy paradigm. The BFO/LSMO films were epitaxially grown on Si(100) by introducing epitaxial layers of $SrTiO_3$/MgO/TiN. X-ray diffraction, scanning electron microscopy, high-resolution transmission electron microscopy, X-ray photo absorption spectroscopy, and atomic force microscopy were employed to fully characterize the samples. Furthermore, we have investigated the magnetic behavior of this five layer heterostructure, in which a d^5 system (Fe^{3+}) manifested in FE-AFM BFO is epitaxially conjoined at the interface to a multivalent transition metal ion such as Mn^{3+}/Mn^{4+} in LSMO. The temperature- and magnetic field-dependent magnetization measurements reveal an unexpected enhancement in magnetic moment and improved magnetic hysteresis squareness originating from the BFO/LSMO interface. We observe a stronger temperature dependence of H_{EB} when the polarity of field cooling is negative as compared to positive field cooling. We believe such an enhancement in magnetic moment and magnetic coupling is likely directly related to an electronic orbital reconstruction at the interface and complex interplay between orbital and spin degrees of freedom, similar to what has previously been reported in the literature. Future work will involve the linearly polarized X-ray absorption measurements to prove this hypothesis. This work represents a starting step toward the realization of magneto-electronic devices integrated with Si(100).

KEYWORDS: *Coerceive field, exchange bias, interface magnetic moment, domain matching epitaxy and multiferroics*

Recently, there have been significant efforts[1,2] exploring the novel physical phenomenon at artificially fabricated oxide heterointerfaces. These studies have revealed a wide range of interesting physical phenomenon with potential applications in magnetic memory, sensors and spintronics. For example, Valencia and coauthors[1] have elegantly demonstrated room temperature (RT) multiferrocity in ultrathin layered films of ferroelectric $BaTiO_3$ with Fe or Co. Another important work by Chakhalian[2] et al. has demonstrated an interface induced orbital ordering and ferromagnetism (FM) driven by charge transfer in a $(Y,Ca)Ba_2Cu_3O_7$ (YBCO) layer deposited onto $La_{0.67}Ca_{0.33}MnO_3$ (LCMO). Finally,[3−5] the formation of novel magnetic states has been demonstrated at the interface of multiferroic $BiFeO_3$ and ferromagnetic $La_{0.7}Sr_{0.3}MnO_3$ when they were deposited on lattice matched $SrTiO_3$ (STO) substrates.

Recently, a great deal of effort has been directed toward the investigation of the properties of lead (Pb)-free multiferroic $BiFeO_3$ (BFO) where ferroelectric (FE) polarization (T_C = 1103 K) and antiferromagnetic (AFM) order (T_N = 643 K)[3−6] coexist. However, the magneto-electric coupling (MEC) in bulk BFO is negligible because of the small net magnetic moment in bulk BFO. Interestingly, the situation changes drastically when BFO is prepared as epitaxial thin films where the FE polarization increases significantly and MEC coupling becomes appreciable.

In particular, there has been widespread interest in utilizing FE-AFM and FM (external)-AFM couplings present in layered films of the multiferroic BFO with FM overlayers to achieve electric-bias induced magnetic moment switching.[7,8] Chu[7] et al. have demonstrated electric field control (E-field) of local FM when BFO is in intimate contact with $Co_{0.9}Fe_{0.1}$, and Lebeugle et al.[8] have reported the demonstration of E-field switching of magnetic anisotropy in Py when it is in contact with BFO. In a more recent work, Wu et al.[3] have shown the reversible electric control of exchange bias (H_{EB}) when BFO was deposited on $La_{0.7}Sr_{0.3}MnO_3$ (LSMO).

These breakthrough investigations reveal interesting novel phenomenon. However, they have only been demonstrated on heterostructures deposited on closely lattice matched insulating substrates such as $DyScO_3$ (DSO), $NdGaO_3$ (NGO), and SrTiO3 (STO). Unfortunately, these substrates are incompatible with the complementary metal-oxide-semiconductor (CMOS)-based technological applications, where Si(100) has

Received: June 27, 2013
Revised: October 22, 2013
Published: November 7, 2013

dx.doi.org/10.1021/nl4023435 | *Nano Lett.* 2013, 13, 5814−5821

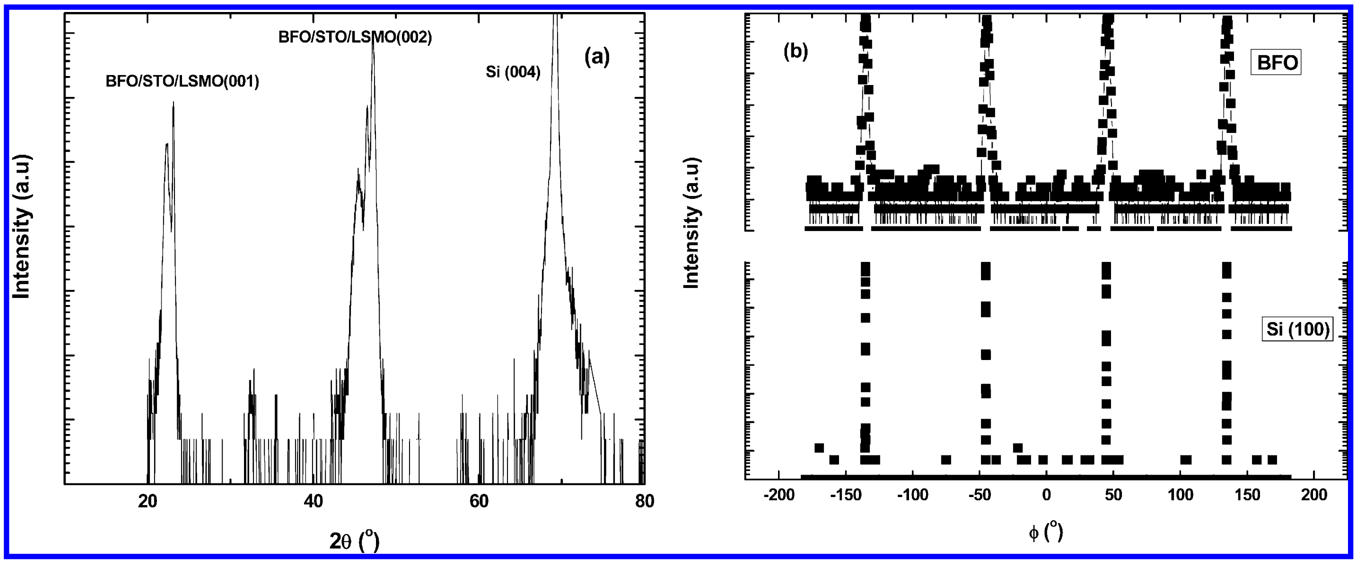

Figure 1. (a) Typical θ-2θ (out of plane) XRD pattern (in log axis) of sample A showing high quality, single phase and (00*l*) films of BFO (b) φ-scan patterns of BFO and Si of (111) reflection collected from sample A at 2θ = 39.46°,ω = 19.73° and χ = 55.00° for BFO and 2θ = 28.46°,ω = 14.23° and χ = 54.74° for Si(100). This pattern shows 4 peaks separated by ~90° indicating its pseudo cubic/rhombohedral symmetry, establishing the cube-on-cube relationship with the underlying substrate Si(100). The φ-scan XRD patterns of LSMO, STO, MgO and TiN layers are shown in the Supporting Information (Figure S1 (a,b,c,)), inferring that all these four layers are epitaxial. The rocking curve with FWHM of 0.7−0.8° of BFO (002) diffraction peak is shown in Supporting Information (see Figure S2).

been the traditional substrate material. In this Letter, we explore the magnetic characteristics of BFO/LSMO interface deposited on Si(100). We have detected an enhancement in magnetic moment, improved squareness in magnetic hysteresis loop, and stronger temperature dependence of exchange bias when the sample is cooled under a negative magnetic field. Such phenomena emanating from the BFO-LSMO interface may be attributed to interface orbital reconstruction, strong coupling of various degrees of freedom and the coupling of ferroelectric domain walls to the interface magnetic moment.

In the current work, we have epitaxially deposited BFO/LSMO heterostructure on Si(100) using pulsed laser deposition (PLD) technique. We accomplish this by involving a unique buffer layer approach using "domain matching epitaxy" (DME)[9] to deposit multilayer oxide-heterostructures on Si(100).[10] A three layer buffer composed of TiN, MgO, and STO was used to accommodate the large lattice mismatches with the Si(100) substrate. The samples studied here were BFO/LSMO/STO/MgO/TiN/Si(100), LSMO/STO/MgO/TiN/Si(100), and BFO/STO/MgO/TiN/Si(100), which we label as sample A, sample B, and sample C, respectively.

Figure 1a presents a θ-2θ X-ray diffraction (XRD) pattern of the five-layer heterostructure of sample A. No evidence of additional phases or interfacial reaction products was observed in the XRD pattern. It is evident from this pattern that all the layers show preferential (00*l*) orientation, suggesting the epitaxial growth of the multilayered structure. From the 2θ XRD data for the (002) peak, we determined the out-of-plane (OOP) lattice parameter of BFO to be 3.966 Å. The epitaxial growth and the in-plane (IP) orientation of all the five layers were studied in detail by means of φ-scan XRD. As depicted in Figure 1b, the φ-scan patterns of (111) reflection for BFO and Si were collected for sample A. This pattern shows four peaks separated by ~90° indicating its pseudo cubic/rhombohedral symmetry and establishing the cube-on-cube relationship of the BFO with the underlying substrate Si(100). The φ-scan XRD patterns of LSMO, STO, and MgO/TiN layers are shown in the Supporting Information (see Figure 1Sa,b,c) confirming that all four layers are grown epitaxially cube-on-cube, that is, (001)Epilayer//(001)Buffer and [100]Epilayer//[100]Buffer. Supporting Information Figure S2 shows the rocking curve of the BFO (002) peak, where the full width at half-maximum (FWHM) is about 0.7−0.8°, comparable to the best BFO films deposited on STO substrates.[11]

Figure 2a is a typical bright-field cross-section transmission electron microscopy (TEM) image of sample A, in which the BFO/LSMO/STO/MgO/TiN/Si(100) layers are labeled. The thicknesses of BFO and LSMO are estimated to be ~100 and 250 nm, respectively. The unmarked top layer belongs to Pt that was sputtered during the focused ion beam (FIB)-sample preparation process. The ⟨110⟩ zone axis electron diffraction pattern of the BFO/LSMO interface is shown in Figure 2b. Because of the excellent match between the lattice constants of BFO and LSMO, their diffraction points for low-index planes overlap with each other. However, we do find the splitting of diffraction points for higher-index planes. For example, the diffraction points corresponding to BFO $(2\bar{2}6)$ and LSMO $(2\bar{2}6)$ planes are distinguishable and labeled in Figure 2b. The alignment of two sets of diffraction spots proves the cube-on-cube epitaxial relationship between the top two layers. It should be emphasized that the epitaxial growth of BFO/LSMO on Si(100) through PLD is possible due to the epitaxial growth of large mismatached system based on the DME paradigm,[9,10] for example, TiN on Si(100) where four lattice constants of TiN match with three of Si(100). An important feature of DME concept is that most of the strain is relieved almost immediately upon initiation of growth, that is, within the first couple of monolayers of growth. In this way, lattice misfit strain accommodation is confined to the interface making it possible for the rest of the film to be grown free of defects and lattice strain. More details on TiN/Si deposition can be found in our earlier work.[12,13] Figure 2c,d shows typical high resolution electron microscopic (HREM) images taken at the BFO/LSMO and LSOM/STO interfaces, respectively. The inset of

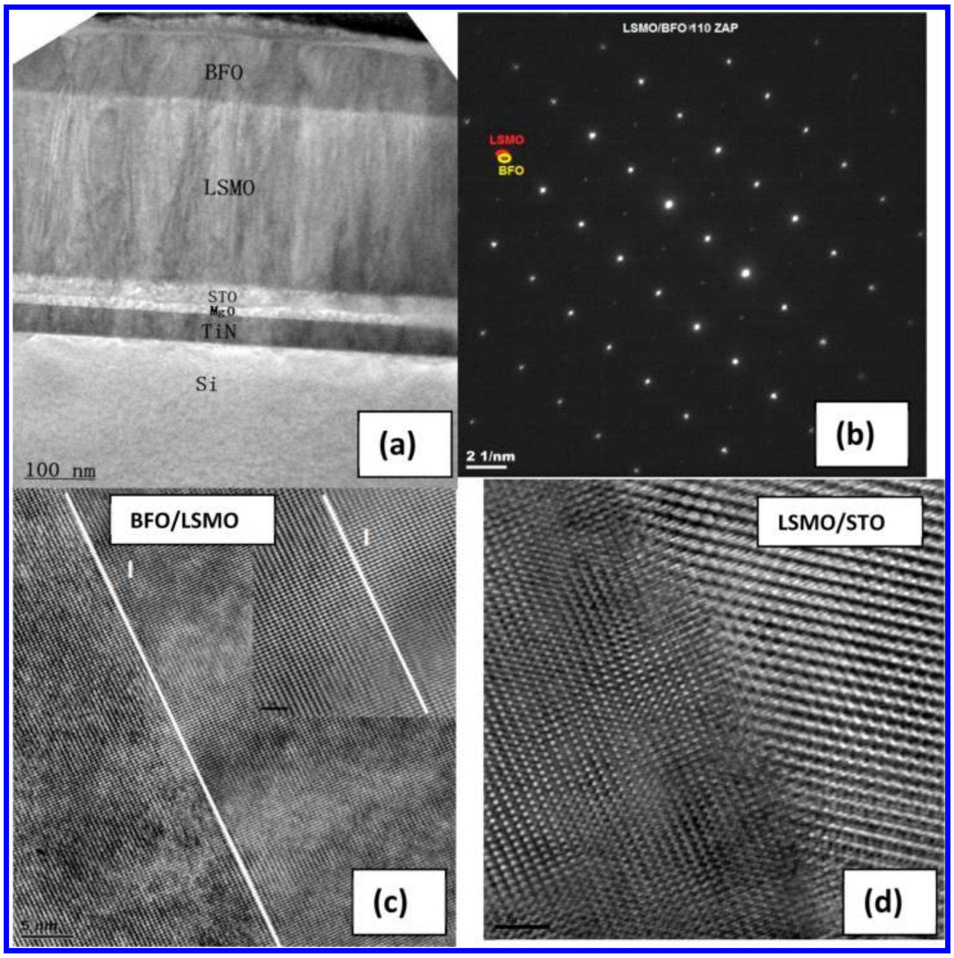

Figure 2. (a) Bright field cross-section TEM image taken from sample A, where BFO (∼100 nm) film was grown at 650 °C. All five-layers are marked. The top unmarked layer is of Pt sputtered during FIB sample preparation process. The scale bar is 100 nm (b) ⟨110⟩ zone-axis pattern (ZAP) for BFO/LSMO interface (c) HRTEM image of BFO (100 nm) /LSMO (250 nm) interface. The inset presents the magnified image, where "I" denotes interface. (d) HRTEM image of LSMO/STO interface. The two interfaces are clean and sharp without interdiffusion and secondary phases.

Figure 2c shows the magnified image across the interface (I) for better clarity. As shown in these images, the interfaces are sharp and clean, with no evidence of interdiffusion or secondary phase formation. A scanning electron microscopic (SEM) image shows a uniform surface of sample A as shown in Figure S3 (see Supporting Information).

As shown in the Supporting Information (see Figure S4), the surface roughness of the films is found to be on the order of ∼7−10 nm, using atomic force microscopy (AFM). Our high resolution X-ray photo absorption spectroscopy (XPS) data (see Supporting Information Figure S5a−c) show fingerprint signatures[14] for the presence of Fe^{3+} with no indication of Fe^{2+}, and no measurable secondary phases such as Bi_2O_3 and Fe_2O_3 or Fe_3O_4, which are known to contribute large leakage currents and unwanted magnetic contributions. Characteristic butterfly loops (of several cycles) were observed (see Supporting Information Figure S6, shown for sample A) in piezoresponse force microscopy amplitude signals of all the BFO films. In addition, the phase signal indicated a clear switching behavior at the switching voltage of 4−5 V, providing unambiguous evidence for the occurrence of ferroelectricity in BFO films.

The magnetic characteristics of samples A, B, and C were investigated as a function of temperature and magnetic field. Field cooling (FC) magnetization versus temperature ($M-T$) curves of samples A (in black), B (in red), and C (blue) are presented in Figure 3. In all the magnetization data shown here, the magnetic field is applied along ⟨100⟩ direction of the sample. The data were collected during the warming cycle under the measuring field of 300 Oe after the samples were cooled under the field of 2000 Oe. As it can be noticed, the Curie temperatures (T_C's) of A and B are found to be the same ∼350 K, consistent with the reported value[15] for LSMO. In addition, there is a crossover in the magnetic moment at around ∼270 K. Below that temperature, the magnetic moment of sample A is greater than that of B. The magnetic moment collected from sample C (no LSMO layer) is much smaller than those of other two structures, consistent with typical AFM behavior of BFO. As discussed in the Supporting Information (see Figure S7), the zero-field cooled (ZFC) and field cooled (FC) (2000 Oe) $M-T$ curves measured on sample A, indicate a blocking temperature of ∼53 K, the temperature at which ZFC and FC curves split.

Isothermal (at 4 K) $M-H$ data were collected on all three samples under ZFC conditions (see Supporting Information, Figure S8). The $M-H$ curves of samples A and B overlap. However, under field cooling it can be seen in Figure 3 that the combination of multiferroic BFO and LSMO (sample A) experiences a large enhancement in magnetic moment and

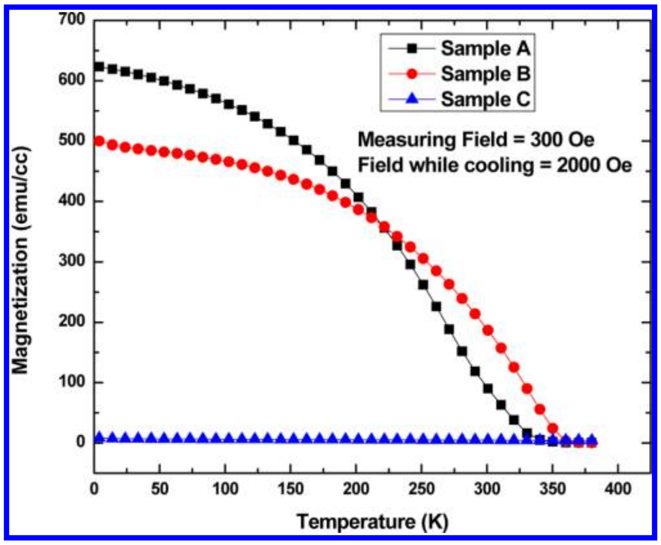

Figure 3. *M*−*T* curves of sample A (in black), sample B (in red), and sample C (in blue) for all the structures. The data were collected during the warming cycle under the measuring field of 300 Oe after the samples had been cooled under the field of 2000 Oe. As it can be noticed, the T_C of sample A and sample B are found to be the same at ~350 K. There is a crossover in the magnetic moment at around ~270 K, whose origin remains unknown. From the ZFC and FC (2000 Oe) *M*−*T* curves, the blocking temperature is found to be ~53 K. Isothermal (at 4 K) *M*−*H* data were collected under ZFC conditions (see Supporting Information, Figures S7, S8). The magnetic field is applied along ⟨100⟩ direction of the sample.

magnetic hysteresis squareness. We interpret this as indicative of the formation of a "ferromagnetic layer" in the BFO sublattice at the interface, as previously reported for similar composite films.[4] In comparison, the isothermal *M*−*H* curve (see Supporting Information Figure S8) for sample C exhibits typical characteristic features[17] of an AFM phase and is consistent with the expectations for BFO deposited on a diamagnetic buffered substrate STO/MgO/TiN/Si(100). We will not discuss the magnetization data collected from sample C further in this work because our primary interest here is to present and discuss the novel magnetic phenomena originating at the BFO/LSMO interface. The consequences of negative and positive field cooling on the magnetic behaviors of sample A and sample B are discussed in the remaining part of this work.

ZFC isothermal (4 K) *M*−*H* measurements, which are presented in Supporting Information (see Figures S7 and S8) on samples A and B, did not reveal the presence of interface magnetic moment. Only when the samples were cooled in the presence of a magnetic field did we observe evidence for the development of an interfacial magnetic moment. Interestingly, we found that the polarity of magnetic field cooling had an effect on the interfacial magnetic moment. To fully investigate this phenomenon, we cooled sample A and sample B down to the measurement temperature under a magnetic field of positive 2000 Oe and negative 2000 Oe. *M* versus *H* data were then collected at several temperatures of 4, 25, 50, 100, 150, 200, 250, and 300 K as they were warmed up to ~370 K (at the end of the each run), the onset of the paramagnetic (PM) phase in LSMO. The excursion to temperatures above T_C at the end of each *M*−*H* measurement was executed to exclude any extrinsic memory effects due to magnetic field- and temperature-excursions. The effects of positive and negative field cooling on magnetic moment, coercive field (H_C), and unidirectional anisotropy, which is in the form of a field bias (H_{EB}), for samples A and B are presented in Figure 4a,b, respectively. As it can be immediately noticed in the FC experiments, the magnetic moment is much greater and the magnetic hysteresis loop is much sharper than that of the ZFC observed for sample A. In addition, there is a clear (though

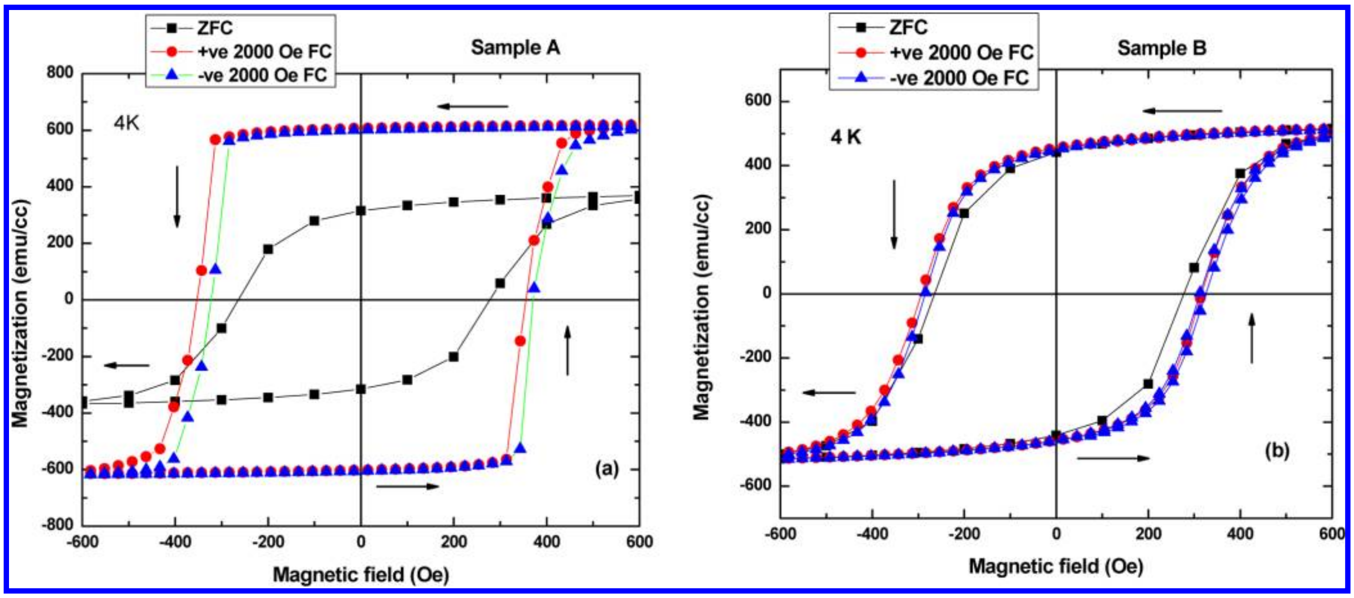

Figure 4. (a) Comparison of isothermal (4 K) *M*−*H* curves measured on sample A under ZFC and after cooling the sample under +2000 Oe, −2000 Oe fields. The magnetic moment in FC case is much higher than ZFC on this sample. Also, there is a shift in FC-*M*−*H* loop. (b) Comparison of isothermal *M*−*H* curves measured on sample B under ZFC and after cooling the sample under +2000 Oe, −2000 Oe fields. Both experiments were conducted under the same conditions as mentioned above. As can be immediately seen, the magnetic moment of sample B practically remains the same, inferring the strong contribution of interface effect of BFO deposited on LSMO. No significant FC-*M*−*H* loop shift and no change in magnetic moment are observed from sample B. The arrows indicate the direction of magnetic field excursion.

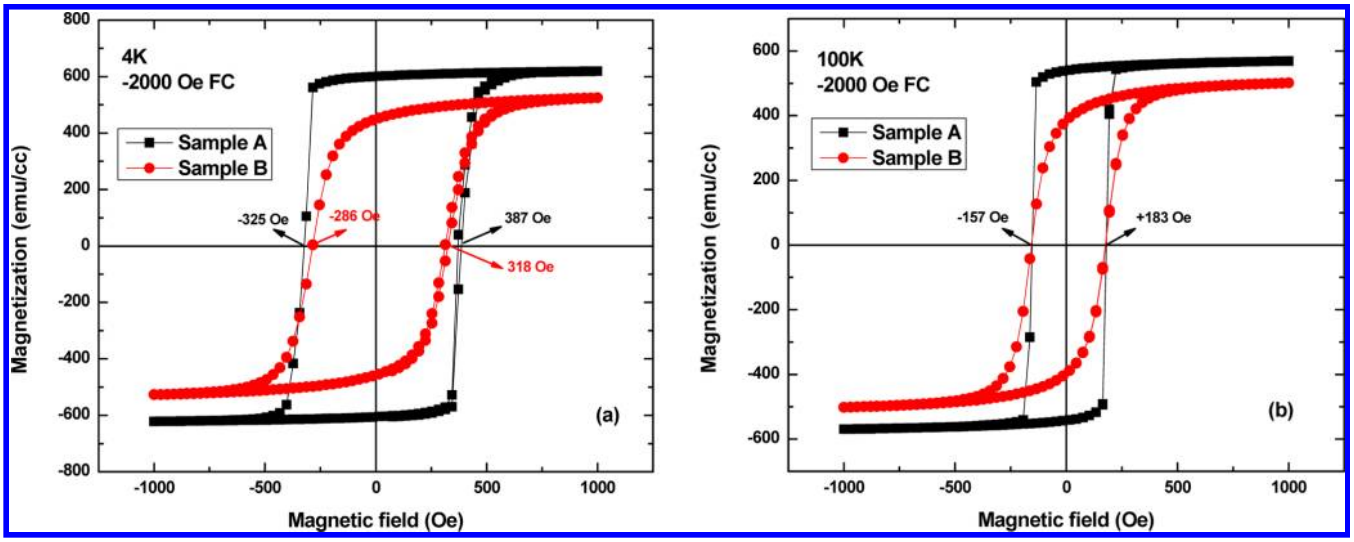

Figure 5. Comparison of negative (−ve) FC (2000 Oe) isothermal (4 K) $M-H$ curves collected on sample A as well as on sample B at (a) 4 K and (b) 100 K. As we can notice immediately, there is a large enhancement in magnetic moment and exchange bias (H_{EB}) of the former sample when compared to the later. As shown in panel b, such curves merged when the data were measured at the temperature of 100 K, above the blocking temperature (T_b) of 53 K (see the Supporting Information, Figure S7). The increase in saturation magnetization for sample A (with BFO) when compared to sample B (without BFO) is ~17% (at 4 K) and 13% (at 100 K).

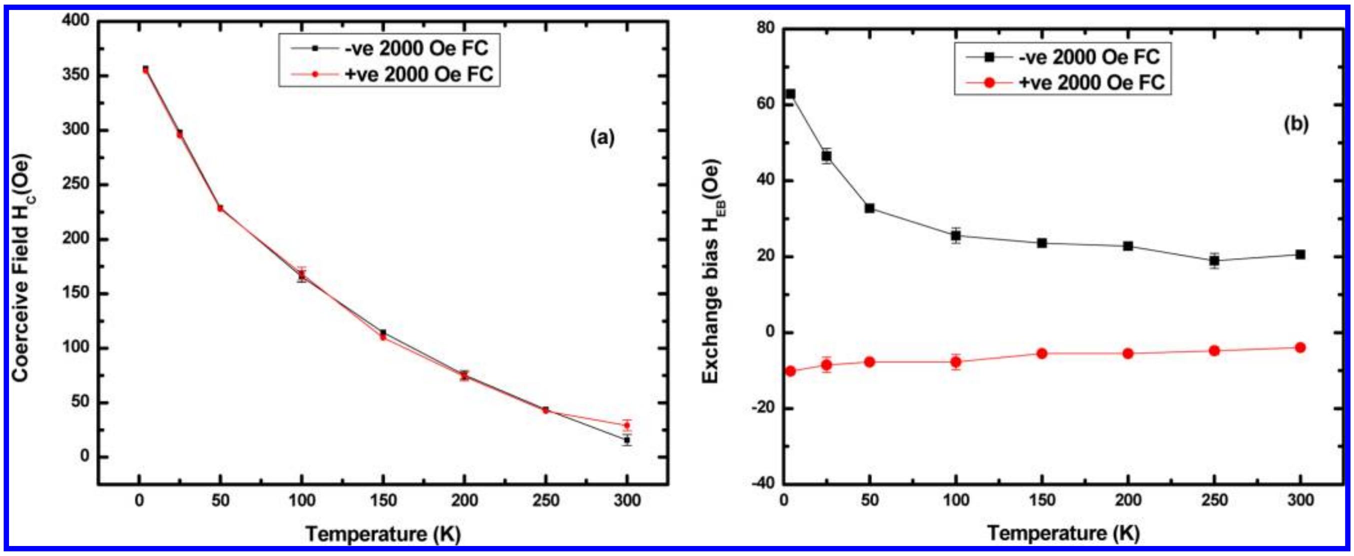

Figure 6. The temperature dependences of (a) H_C and (b) H_{EB} obtained when the sample A was positive (in red) and negative (in black) field cooled under 2000 Oe from 370 K (PM phase). Lines guide the eye. The temperature dependences of H_C are the same in both the cases, that is, decreases with the increase in temperature. Interestingly, the temperature dependence of H_{EB} is much stronger in negative field cooled case when compared to positive field cooling. The error bars are estimated from the multiple measurements.

small) horizontal shift (H_{EB}) in the FC $M-H$ loop. These differences are not observed for sample B. As it can be immediately seen (see Figure 4b), the magnetic moment of sample B obtained under all three experimental protocols remains nearly identical.

Next, we show the effect of negative field cooling between sample A and sample B recorded at two distinct temperatures 4 and 100 K, below and above the blocking temperature (T_b), respectively. Figure 5 compares the negative FC (2000 Oe) $M-H$ data collected from sample A (in black) and sample B (in red). As we can notice immediately, there is a large enhancement in magnetic moment and exchange bias (H_{EB}) for sample A in comparison with sample B. As shown in Figure 5b, the curves for sample A merge when the data are measured at 100 K, which is above the blocking temperature (T_b) of 53 K. In addition, the squareness of magnetic hysteresis loop measured both above and below T_b has increased when LSMO layer is in intimate contact with BFO layer. We notice a similar behavior when both samples were cooled in +2000 Oe (not shown). Interestingly, when the sample A is negatively field cooled we find a stronger temperature dependence on H_{EB}, which diverges markedly as the sample is cooled below T_b.

Temperature dependences of H_c and H_{EB} measured under positive and negative field cooled conditions provide complementary insight into the nature and mechanism of coupling in these heterostructures. Figure 6a,b compares the temperature dependences of H_C and H_{EB} that resulted when the sample A was negatively and positively field cooled in 2000 Oe. These measurements reveal a number of interesting aspects. As shown in Figure 6a, regardless of sign of field cooling, sample A shows an increase in H_C as the temperature decreases and a similar temperature dependence. The H_C is as high as 350 Oe at 4 K and then decreases with increasing temperature. Figure 6b presents the temperature dependences of H_{EB} for sample A as it was under positive and negative magnetic field cooling. As is evident, the temperature dependence of H_{EB} is much stronger for negative field cooling case. From Figure 6b, an H_{EB} of ~62 Oe is noticed at 4 K when the sample is negatively field cooled, which decays (exponentially) as a function of increasing temperature. In contrast, an H_{EB} of ~10 Oe and a much weaker temperature dependence is measured at 4 K when the sample is cooled in a positive field. It should be noted that in an atomic moment picture of the G-type AFM structure (all nearest-neighbor spins are anti parallel)[16] of BFO, the (001) surface is expected to be fully magnetically compensated and thus give rise to no H_{EB}. The present data may suggest that in our case, a new magnetic structure may be presenting at the interface with LSMO, that may differ markedly from that found in the bulk of the BFO film. The importance of the interface is clearly demonstrated when a thin layer of ~10 nm nonmagnetic STO is inserted between BFO and LSMO resulting in a complete quenching (not shown) of H_{EB}.

Similar results have been reported in the literature previously, while exploring the uniaxial magnetic anisotropy in LSMO/BFO thin film heterostructure deposited on 0.2° miscut STO(001) substrate prepared by PLD. You[17] et al. observed a nearly identical but opposite effect for the case where LSMO was deposited on BFO. That is, the magnetic moment of the double layer LSMO/BFO film was lower when compared to that of single layer film LSMO. This observation was explained in terms of a strain induced layer that formed in BFO layer through a Jahn−Teller (JT) effect in response to the strain introduced by top LSMO layer. Following the analogy reported in the literature,[4] the enhancement in magnetic moment and H_{EB} after deposition of BFO on top of LSMO may be due to the strong coupling of the ferroelectric domains in BFO with the magnetic moment in LSMO that occurs within the first few monolayers of interface in the BFO sublattice.

The interesting question centers on why the temperature dependence of H_{EB} is stronger when the sample is negatively field cooled. Our observations are consistent with the recent work done by Wu[3] et al., in which they reported for a BFO/LSMO heterostructure that the magnitude of H_{EB} is higher and has a stronger temperature dependence when BFO is negatively polarized, and lower with a weaker temperature dependence when the BFO is positively polarized by an applied electric field (see Figure 3 in ref 5). They attributed this behavior to the presence of both pinned and rotatable spins at the interface. Similar results have been reported for CoFe/BFO heterostructures.[16,18,19] In particular, Bea[16] et al. analyzed the H_{EB} in the CoFeB/BFO system and found that H_{EB} scales with the inverse width of the FE and AFM domains in (001)-oriented BFO films, in agreement with the Malozemoff's model[20] for atomically rough interfaces. In this case, the net magnetic moment is found to present within 2 nm region in the BFO sublattice at the interface. Finally, Dong and co-workers have proposed[21] that the Dzyaloshinskii-Moriya and super exchange interactions could induce H_{EB} at the interface in FM/G-type AFM (multiferroic) oxides heterostructures. In addition, they argue that for FM/G-type AFM heterostructures, such as LSMO/BFO, extrinsic factors such as interface roughness could also influence H_{EB}. Some combination of similar mechanisms may be acting in the present case, as well, although its proof would clearly require additional measurements and theoretical calculations. We note that these experimental findings notwithstanding, our studies are still at an early stage in our understanding of these heterostructure interfaces. In our future experimental work, we plan to examine the details of the factors such as BFO surface roughness, the thickness of BFO and LSMO layers, magnitude of applied magnetic field cooling during magnetization measurements. We believe these factors ultimately determine the strengths of various magnetic interactions and order parameters, particularly at the interface.

In summary, we have successfully grown BFO/LSMO on Si(100) using STO/MgO/TiN buffer layers via domain matching epitaxy, deposited by pulsed laser deposition method. All five layers have been grown epitaxially without any measurable secondary phases. Our comprehensive magnetization data infer an enhancement in magnetic moment, squareness and exchange bias when antiferromagnetic ferroelectric BFO is placed in contact with ferromagnetic LSMO. The exchange bias is found to show a stronger temperature dependence when the sample is cooled in negative field. Our experimental results are consistent with the formation of new ferromagnetic phase in the BFO sublattice brought on by magnetic reconstruction at the interface. We plan to measure the magnetic spin structure of BFO and nature of spin coupling between Fe^{3+} and $Mn^{3+/4+}$ at the heterointerface using XMCD and PEEM techniques, which may provide interface-specific information. The current work is the key step toward the integration of magneto-electronic devices with Si(100) exploring interface magnetsm with dissimilar materials.

Methods Summary. Here, we summarize the experimental methods used in this study. Pulsed laser deposition (PLD) was used to grow the epitaxial layers on Si(100) substrate in this work. In the current work, we have grown BFO/LSMO/STO/MgO/TiN/Si(100) heterostructures and optimized the growth conditions for each layer in this geometry. This work is facilitated by the deposition of an epitaxial TiN (a = 4.24 A°). Three lattice constants of Si (a = 5.43 A°) match very well with four of TiN (a = 4.24 A°) and the epitaxial growth occurs via DME. Each layer in this heterostructure was grown epitaxially. This buffer layer consists of TiN, MgO (a = 4.22 A°), and STO (a = 3.905 A°). TiN was chosen because it grows epitaxially on Si(100) and has superior diffusion barrier properties. TiN has an excellent lattice match with MgO, which has a misfit of about 8% with STO. Lattice constant of STO (3.905 A°) matches closely with that of LSMO (3.85 A°) and BFO (3.966 A°). This unique selection of buffer layers made it possible to integrate epitaxial thin film of BFO/LSMO on Si(100).

The PLD chamber comprises of multitarget assembly for holding four targets with a facility to rotate and position any target of interest in line with the laser beam. This assembly allows the target to rotate continuously to provide uniform ablation. The substrate mounting assembly is comprised of a radiation heater, a Mo plate for mounting the substrate, and a thermocouple for measuring substrate temperature. A Lambda Physik (LPX200) pulsed KrF excimer laser beam (wavelength λ = 248 nm, pulse width τ = 25 ns, repetition rate 5−10 Hz) is incident on the target at an angle close to 45° with a spot size around 1 mm ×4 mm. The distance between the target and the substrate was kept between 45 and 50 mm.

Prior to the deposition, the chamber is evacuated to a pressure less than 1× 10^{-6} Torr using a combination of a mechanical pump and turbo molecular pump. The Si(100) substrates were cleaned in acetone and methanol baths in an ultrasonic container and then dipped in 20% HF solution for a minute to remove the native surface oxide. We have used TiN, MgO, STO, and LSMO targets which were all stoichiometric and pure, typically 99.9%. Following the literature-reported procedure,[5] the BFO target was made with 10% excess Bi to compensate for Bi loss during deposition, as Bi has a much higher vapor pressure.

TiN, MgO, and STO targets were ablated sequentially in the same run. The deposition of TiN film was done at 625 °C in vacuum (1×10^{-6} Torr). After TiN deposition, the first few mono layers (for about 500 pulses) of MgO were deposited under vacuum (1×10^{-6} Torr) at 575 °C. The remaining MgO was deposited at the same temperature in the oxygen pressure of 6×10^{-4} Torr. For STO deposition the substrate temperature was raised to 700 °C and oxygen pressure to 3×10^{-3} Torr. For LSMO and BFO depositions, the substrate temperature was kept at 650 °C and oxygen pressure was 2×10^{-1} and 5×10^{-2} Torr, for these depositions, respectively. The energy density and pulse frequency were 1.5− 3 J/cm^2 and 10 Hz, respectively. The samples were cooled slowly under O_2 pressure of 5×10^{-2} Torr.

A Rigaku SmartLab X-ray diffractometer with a Bragg−Brentano Goniometer (copper X-ray anode, Kα radiation, λ = 0.154 nm) was employed for θ-2θ scan to determine the structure, crystallinity and out-of-plane orientation of the films. In addition, a PANalytical Empyrean X-ray diffractometer, equipped with a high resolution goniometer (minimum step size =0.0001) was used for φ-scan X-ray diffraction (XRD) to determine the in-plane orientation of the films. Parallel beam geometry was selected on the primary side and a 0.18° PPC slit was used for the secondary optics. Microstructural studies were carried out employing JEOL 2010F high-resolution/analytical transmission electron microscope (TEM), operated at 200 KV, with a point-to-point resolution of 1.8 A°. The single crystalline nature, interface quality and the proposed epitaxial relationships were confirmed by selected area electron diffraction (SAED) of cross sections of the sample. The TEM sample was prepared by a focused ion beam (FIB) technique.

SPECS-made XPS spectrometer with Al/Mg anode source was used for the surface elemental analysis and to identify the Fe valence state. Digital Instruments D3000 AFM equipped with Si cantilever coated with Ti/Ir was used under tapping mode option to image the surface topography and to measure film surface roughness. To probe ferroelectric characteristics at room temperature, we have used switching spectroscopy piezoresponse force microscopy (SSPFM) technique. For this purpose, the commercial scanning probe microscope (Cypher, Asylum Research) equipped with a Pt-coated conducting tip (AC240TM, Olympus) was operated at the resonance frequency of about 260 kHz and the ac bias amplitude of 2 V. The same setup was augmented to carry out advanced SSPFM measurements. We used a 25 × 25 grid on 2 μm × 2 μm scan area to map the local polarization switching with variable tip bias between +7 and −7 V.

The temperature- and magnetic-field dependent magnetization measurements were carried out using Quantum design MPMS SQUID VSM dc magnetometer with the sensitivity $\leq 10^{-8}$ emu at 0 T (T). It should be noted that TiN, MgO and STO buffer layers are all nonmagnetic, and hence, are not expected to contribute to the magnetic properties of BFO/LSMO heterostructures that are presented in this work. The deposition parameters have been kept the same to maintain the same thicknesses of TiN, MgO, STO, BFO and LSMO layers in all three samples studied here. For magnetization measurements, a piece of ~4 mm ×5 mm was used from each sample. In all the measurements reported here, the magnetic field is applied parallel to the film plane. The magnetic field paths followed were 0→10,000→0→-10,000→0→10,000 Oe in the zero field cooled for (M−H) run; and 0→1000→0→-1000→0→1000 Oe for positive and negative field cooled M−H measurements collected from sample A and sample B. The same sequence was followed at each temperature for all samples to provide a meaningful comparison. Great care was taken not to contaminate the samples while measurements were being performed.

■ ASSOCIATED CONTENT

Ⓢ Supporting Information

Figures S1−S8. This material is available free of charge via the Internet at http://pubs.acs.org.

■ AUTHOR INFORMATION

Corresponding Author

*E-mail: ssingam@ncsu.edu.

Notes

The authors declare no competing financial interest.

■ ACKNOWLEDGMENTS

SSR acknowledges National Academy of Science (NAS), USA for awarding the NRC postdoctoral research associate fellowship. We thank N Sudhakar and P Gupta for their valuable experimental help. The authors are pleased to acknowledge the support of the Army Research Office under Grant W911NF-04-D-0003. Also, the authors acknowledge the use of the Analytical Instrumentation Facility (AIF) at North Carolina State University, which is supported by the State of North Carolina and the National Science Foundation.

■ REFERENCES

(1) Valencia, S.; Crassous, A.; Bocher, L.; Garcia, V.; Moya, X.; Cherifi, R. O.; Deranlot, C.; Bouzehouane, K.; Fusil, S.; Zobelli, A.; Gloter, A.; Mathur, N. D.; Gaupp, A.; Abrudan, R.; Radu, F.; Barthélémy, A.; Bibes, M. *Nat. Mater.* **2011**, *10*, 753.

(2) Chakhalian, J.; Freeland, J. W.; Habermeier, H.-U.; Cristiani, G.; Khaliullin, G.; van Veenendaal, M.; Keimer, B. *Science* **2007**, *318*, 1114.

(3) Wu, S. M.; Cybart, S. A.; Yu, P.; Rossell, M. D.; Zhang, J. X.; Ramesh, R.; Dynes, R. C. *Nat. Mater.* **2010**, *9*, 756.

(4) Yu, P.; Lee, J.-S.; Okamoto, S.; Rossell, M. D.; Huijben, M.; Yang, C.-H.; He, Q.; Zhang, J. X.; Yang, S. Y.; Lee, M. J.; Ramasse, Q. M.; Erni, R.; Chu, Y.-H.; Arena, D. A.; Kao, C.-C.; Martin, L. W.; Ramesh, R. *Phys. Rev. Lett.* **2010**, *105*, 027201.

(5) Wu, S. M.; Cybart, S. A.; Yi, D.; Parker, J. M.; Ramesh, R.; Dynes, R. C. *Phys. Rev. Lett.* **2013**, *110*, 067202.

(6) Eerenstein, W.; Mathur, N. D.; Scott, J. F. *Nat. Mater.* **2006**, *442*, 759.

(7) Chu, Y.-H.; Martin, L. W.; Holcomb, M. B.; Gajek, M.; Han, S.-J.; He, Q.; Balke, N.; Yang, C.-H.; Lee, D.; Hu, W.; Zhan, Q.; Yang, P.-L.; Fraile-Rodríguez, A.; Scholl, A.; Wang, S. X.; Ramesh, R. *Nat. Mater.* **2008**, *7*, 478.

(8) Lebeugle, D.; Mougin, A.; Viret, M.; Colson, D.; Ranno, L. *Phys. Rev. Lett.* **2009**, *103*, 257601.

(9) Narayan, J.; Larson, B. C. *J. Appl. Phys.* **2003**, *93*, 278. Narayan, J. *Acta Materialia* **2013**, *61*, 2703.

(10) Tiwari, A.; Jin, C.; Narayan, J. *Appl. Phys. Lett.* **2002**, *80*, 4039.

(11) Dho, J.; Qi, X.; Kim, H.; MacManus-Driscoll, J. L.; Blamire, M. G. *Adv. Mater.* **2006**, *18*, 1445.

(12) Narayan, J.; Tiwari, P.; Chen, X.; Singh, J.; Chowdhury, F. L.; Zheleva, T. *Appl. Phys. Lett.* **1992**, *61*, 1290.
(13) Narayan, J. *US Patent #* 5406123 (1995).
(14) Eerenstein, W.; Morrison, F. D.; Dho, J.; Blamire, M. G.; Scott, J. F.; Mathur, N. D. *Science* **2005**, *307*, 1203a.
(15) Lee, J.-S.; Arena, D. A.; Yu, P.; Nelson, C. S.; Fan, R.; Kinane, C. J.; Langridge, S.; Rossell, M. D.; Ramesh, R.; Kao, C.-C. *Phys. Rev. Lett.* **2010**, *105*, 257204.
(16) Béa, H.; Bibes, M.; Ott, F.; Dupé, B.; Zhu, X.-H.; Petit, S.; Fusil, S.; Deranlot, C.; Bouzehouane, K.; Barthélémy, A. *Phys. Rev. Lett.* **2008**, *100*, 017204.
(17) You, L.; Lu, C.; Yang, P.; Han, G.; Wu, T.; Luders, U.; Prellier, W.; Yao, K.; Chen, L.; Wang, J. *Adv. Mater.* **2010**, *22*, 4964.
(18) Martin, L. W.; Chu, Y.-H.; Holcomb, M. B.; Huijben, M.; Yu, P.; S-J Han, S.-J.; Lee, D.; Wang, S. X.; Ramesh, R. *Nano Lett.* **2008**, *8*, 2050.
(19) Trassin, M.; Clarkson, J. D.; Bowden, S. R.; Liu, J.; Heron, J. T.; Paull, R. J.; Arenholz, E.; Pierce, D. T.; Unguris, J. *Phys. Rev. B* **2013**, *87*, 134426.
(20) Malozemoff, A. P. *Phys. Rev. B* **1987**, *35*, 3679.
(21) Dong, S.; Yamauchi, K.; Yunoki, S.; Yu, R.; Liang, S.; Moreo, A.; Liu, J.-M.; Picozzi, S.; Dagotto, E. *Phys. Rev. Lett.* **2009**, *103*, 127201.